Article:

Parks, MM, Heimisson, ER, Sigmundsson, F et al. (16 more authors) (2017) Evolution of deformation and stress changes during the caldera collapse and dyking at Bárdarbunga, 2014–2015: Implication for triggering of seismicity at nearby Tungnafellsjökull volcano. Earth and Planetary Science Letters, 462. pp. 212-223. ISSN 0012-821X

https://doi.org/10.1016/j.epsl.2017.01.020

Evolution of deformation and stress changes during the caldera collapse and dyking at Bárdarbunga, 2014-2015: Implication for triggering of seismicity at nearby Tungnafellsjökull volcano

Michelle Maree Parks[1], Elías Rafn Heimisson[2], Freysteinn Sigmundsson[1], Andrew Hooper[3], Kristín Vogfjörd[4], Thóra Árnadóttir[1], Benedikt Ófeigsson[4], Sigrún Hreinsdóttir[5], Ásta Rut Hjartardóttir[1], Páll Einarsson[1], Magnús Tumi Gudmundsson[1], Thórdis Högnadóttir[1], Kristín Jónsdóttir[4], Martin Hensch[4], Marco Bagnardi[3], Stéphanie Dumont[1], Vincent Drouin[1], Karsten Spaans[3], Rósa Ólafsdóttir[1].

[1]Nordic Volcanological Center, Institute of Earth Sciences, University of Iceland, Reykjavík, Iceland.

[2]Department of Geophysics, Stanford University, Stanford, California, USA.

[3]COMET, School of Earth and Environment, University of Leeds, Leeds, UK.

[4]Icelandic Meteorological Office, Reykjavik, Iceland.

[5]GNS Science, Lower Hutt, NZ.

Corresponding author: Michelle Parks, michelle@hi.is

Highlights

- Constrained multi-source model reproduces both the near- and far-field volcanic deformation
- Temporal evolution of source parameters determined throughout unrest and eruption

- Bárdarbungna caldera collapse triggers earthquakes at nearby Tungnafellsjökull volcano

Abstract

Stress transfer associated with an earthquake, which may result in the seismic triggering of aftershocks (earthquake-earthquake interactions) and/or increased volcanic activity (earthquake-volcano interactions), is a well-documented phenomenon. However limited studies have been undertaken concerning volcanic triggering of activity at neighbouring volcanoes (volcano-volcano interactions). Here we present new deformation and stress modelling results utilising a wealth of diverse geodetic observations acquired during the 2014-2015 unrest and eruption within the Bárdarbunga volcanic system. These comprise a combination of InSAR, GPS, LiDAR, radar profiling and optical satellite measurements. We find a strong correlation between the locations of increased seismicity at nearby Tungnafellsjökull volcano and regions of increased tensile and Coulomb stress changes. Our results suggest that stress transfer during this major event has resulted in earthquake triggering at the neighbouring Tungnafellsjökull volcano by unclamping faults within the associated fissure swarm. This work has immediate application to volcano monitoring; to distinguish the difference between stress transfer and new intrusive activity.

Keywords

Joint inversion of geodetic observations; Holuhraun eruption; Bárdarbunga; Tungnafellsjökull; stress triggering; subsurface fault mapping.

1 Introduction

An earthquake can increase rates of seismicity on surrounding faults by altering the shear and normal stress fields (e.g., King et al, 1994; Stein et al., 1992; Harris and Simpson, 1992) via both increased shear and unclamping, which are related to changes in Coulomb failure stress (Stein, 1999). Abrupt changes in pressure within a magmatic system may also be induced by nearby earthquakes, ultimately leading to an eruption (e.g. Walter and Amelung, 2007; Manga and Brodsky, 2006; Hill et al., 2002; Marzocchi et al., 2002; Linde and Sacks, 1998). Conversely, volcanic activity may trigger earthquakes on near-by faults (e.g. Hill et al., 2002; Roman and Heron, 2007; Jónsson, 2009; Green et al., 2015; Heimisson et al., 2015). Numerous studies have been undertaken on stress transfer during earthquake-earthquake interactions (e.g. Freed 2005; Árnadóttir et al., 2003; Stein, 1999 and references therein) along with earthquake-volcano interactions (e,g, Walter and Amelung, 2007; Parsons et al., 2006; Díez et al., 2005; Toda et al., 2005; La Femina et al., 2004; Hill et al., 2002; Nostro et al., 1998). However, fewer studies have investigated volcanic stress triggering at neighbouring volcanoes (e.g., Albino and Sigmundsson, 2014; Gonnermann et al., 2012).

In this work we study the interaction between two closely spaced (25 km) central volcanoes in Iceland, Bárdarbunga and Tungnafellsjökull. The volcanoes are very different. Bárdarbunga is one of the most powerful volcanoes in Iceland, with at least 26 eruptions in the last 1100 years, including four where the magma volume was between 1 and 4 km^3. Its associated fissure swarms extend 115 km to the southwest and at least 55 km to the north of the volcano (Larsen and Gudmundsson, 2015; Hjartardóttir et al., 2016). Tungnafellsjökull, on the other hand, has only had two minor eruptions in the Holocene, and its fissure swarms are immature, extending only

25 km to the southwest and 15 km to the north of the volcano (Einarsson, 2015; Björnsdóttir and Einarsson, 2013). Compared to the Bárdarbunga volcano, Tungnafellsjökull has not been very seismically active over the last 26 years of digital seismic recording in Iceland, with a yearly average of two recorded earthquakes of M≥2. However, seismicity at Tungnafellsjökull increased at the same time as major unrest, dyke propagation, slow caldera collapse and eruption occurred within the Bárdarbunga volcanic system, Iceland (Figure 1). We can gain insight into volcano interactions during these events by the joint analysis of earthquake and ground deformation data.

Major activity in the Bárdarbunga volcanic system was initially identified by the onset of an intense earthquake swarm on the 16th August 2014 and concurrent movement registered at several nearby continuous GPS (cGPS) stations. Over the following weeks additional cGPS stations were installed, campaign GPS sites were reoccupied and interferograms formed using X-band and C-band satellite images. Data were analysed in near real-time and used to map ground displacements associated with the initial dyke emplacement and propagation (northeast of Bárdarbunga caldera), responsible for the sudden unrest (Sigmundsson et al 2015). The main fissure eruption commenced on the 31st August, characterised by lava fountaining and the extrusion of extensive lava flows. In addition to the lava effusion, a slow collapse of the Bárdarbunga caldera began on the 20th August 2014 (Gudmundsson et al., 2016) and continued throughout the eruption, resulting in a maximum subsidence of 65 m by the end of the eruption on the 27th February 2015. Shortly after the onset of unrest at Bárdarbunga (within 24 hours), an increase in seismicity was observed at the neighbouring Tungnafellsjökull volcano situated ~25 km northwest of the Bárdarbunga caldera (Figures 1 and 2). The seismicity however abruptly increased during unrest in Bárdarbunga; to 10 times the average in 1996 and to 60 times the average in 2014.

Possible mechanisms for increased seismicity at Tungnafellsjökull during the 2014-2015 Bárdarbunga unrest and eruption include:

1) A new intrusion beneath Tungnafellsjökull volcano,
2) Pressure change within a resident magma body beneath Tungnafellsjökull,
3) Dynamic stress transfer related to the passing of seismic waves from large Bárdabunga earthquakes,
4) Static stress transfer related the Bárdarbunga unrest and eruption.

Activity in the magmatic system of the receiver volcano (Tungnafellsjökull) would be responsible for possibilities (1) and (2), whereas the origin of the seismicity would be related to activity in the source volcano (Bárdarbunga) for cases (3) and (4). In order to consider case (4), three distinct deformation processes need to be considered in the Bárdarbunga volcanic system: i) dyke propagation from Bárdarbunga caldera to the Holuhraun eruption site (deformation associated with this emplacement continued from 16th August 2014 to mid September 2014), ii) magma withdrawal from a reservoir ~12±4 km beneath the caldera (Gudmundsson et al., 2016) and iii) slow caldera collapse. Processes ii) and iii) continued throughout the eruption.

Previous deformation and stress modelling studies have been undertaken in the vicinity of Bárdarbunga during the 2014-2015 activity. Sigmundsson et al. (2015) originally modelled the complex deformation field, associated with the lateral dyking event and the associated caldera collapse, during the initial period of activity from 16th August to 6th September 2014. A Markov chain Monte Carlo (MCMC) approach was used to estimate the multivariate probability distribution of opening and shearing on a segmented dyke, extending from the southeast edge of the caldera to the eruption site, slip on two caldera faults, and deflation of either a spherical or flat-topped magma chamber at depths of ~1.4 and 3.5 km BSL respectively. Riel at al. (2015), modelled the caldera subsidence utilising InSAR observations spanning the first few weeks of the eruption. The magma chamber was modelled as a deflating horizontal circular crack in an elastic half-space. The authors concluded that one of the most likely physical processes responsible for the large number of CLVD (compensated linear vector dipole) dominant M5 earthquakes accompanying the collapse, was slip on caldera ring faults. They compared deformation associated with a M4.9 earthquake, in the northern sector of the caldera on the 14th September (derived from 1-day interferograms), with a static model of slip on a 1 km wide ring fault segment at a depth of 2 km. Green et al. (2015) investigated the static stress changes associated with dyke emplacement and deflation of a source at 17 km BSL beneath Bárdarbunga caldera. They demonstrated a stress shadow effect within regions to the north and east of the volcano. More recently Gudmundsson et al. (2016), used a combination of distinct element method numerical modelling and seismic data to run a series of forward simulations of the magma chamber and ring fault system, which were compared to a NNW-SSE trending caldera subsidence profile (collected using radar altimetry and corrected for ice-flow). They determined that the subsidence at depth was controlled by the reactivation of steeply dipping ring faults.

Our study incorporates a similar ring fault and magma reservoir geometry as Gudmundsson et al. (2016) combined with the dyke geometry from Sigmundsson et al. (2015). We undertake a joint inversion of multiple geodetic datasets (caldera subsidence grids, GPS and InSAR observations) using a Bayesian approach and present a new constrained model of the subsurface processes within the Bárdarbunga volcanic system. Our model reproduces the complete cumulative deformation field for six individual time periods between 16th August 2014 and 10th April 2015 (Figure 2). In addition, we generate a time series of cumulative stress changes throughout the period of volcanic unrest and eruption, and compare our results to earthquake relocations and mechanisms at the neighbouring Tungnafellsjökull volcano, to ultimately determine the most likely cause of the increased seismicity in that area.

2 Data and methods

The input data to our modelling comprises a combination of various seismic and geodetic observations. We utilise a more diverse dataset than those presented in previous Bárdarbunga deformation studies. This consists of both near- and far-field deformation measurements spanning an extended time period (16th August 2014 to 10th April 2015). These data include both campaign and GPS observations from 33 stations with good azimuthal coverage around Bárdarbunga (Figure 1 and Table S1 in Supplementary Material), subsidence grids covering the caldera (derived from a combination of LiDAR, radar altimetry and SPOT datasets), and X-band interferograms (see Table S2 in Supplementary Material). Detailed descriptions of the methods used to process these data are outlined in section S3 (Supplementary Material). Information regarding the earthquake hypocenter relocations, deformation modeling and stress modeling is included in the following section.

2.1 Earthquake hypocenter relocations

High-precision relocations of earthquakes within the Tungnafellsjökull central volcano, recorded by the Icelandic national digital seismic network - South Iceland Lowland (SIL) network - (Böðvarsson et al., 1996; 1999), were used to locate the active areas within the volcano during the 2014-2015 Bárdarbunga unrest and eruption, and where possible, to map the active faults and fractures and their slip directions. Over 750 earthquakes in the Tungnafellsjökull area between 2008 and March 2015 are relocated using the relative, double-difference method of Slunga et al. (1995) and the standard SIL velocity model generally used for initial routine locations of earthquakes in Iceland (Stefánsson et al., 1993).

The relocated event distribution displayed in Figure 1c shows that the activity is mostly distributed in a southwest-northeast direction, extending from the central part of the Tungnafellsjökull caldera to the area north of it and in a small cluster in Vonarskard caldera. Almost 90% of events are at depths < 9 km, 66% at depths < 5 km. Source depths of event clusters appear to increase towards north; from a maximum of 4 km in the south to 8.5 km in the north. The bulk of the activity at Tungnafellsjökull also moves with time from south to north during the Bárdarbunga unrest, while the cluster in Vonarskard is active throughout the period. Absolute accuracy of events strongly depends on the availability of observations from close-in stations, therefore events prior to the installation of the Vonarskard station in 2011 and during times of its outages in December 2014 through January 2015 have less constrained source depths. This outage appears to affect the depth accuracy of the latest events in the Vonarskard cluster – concentrated at 7-8 km depth, while the previous events cluster at 3-4 km depth – and the clusters north of Tungnafellsjökull, which all have depths extending down to around 8 km. The absolute depths of these northernmost clusters are therefore uncertain and likely to be overestimated by 2–4 km.

Many small lineaments and fractures are illuminated by the relocated seismicity. The 10 main fractures outlined by the event distribution are displayed in Figure S4 (Supplementary Material). These are jointly interpreted with the distribution of individual focal mechanisms to define the strike, dip and approximate slip direction on each fault (Table S5 in Supplementary Material). Most of the mapped faults strike in a similar direction as the long-axis of the caldera and most faults within the caldera dip around 55 degrees to northwest, whereas faults at the northern margin and north of the caldera are closer to vertical and have a more varied strike. Slip directions are mostly normal or close to normal, except for a near-vertical fault at the eastern caldera rim, active in 2012, where slip direction is close to left-lateral strike slip. This fault was not reactivated in 2014-2015. The northernmost fault segment (Supplementary Material Figure S4, segment nr. 5) is just southeast of a surface fault mapped from aerial photographs (Björnsdóttir and Einarsson, 2013) with a similar strike. The general consistency of the orientation and slip direction of the fault plane solutions suggests that in spite of the rather large azimuthal gap in the northwest quadrant of Tungnafellsjökull, the mechanisms are rather well constrained.

2.2 Deformation modelling

We generated a series of deformation models covering the period 16th August 2014 to 10th April 2015. Each of these models comprise i) a sill, at depth beneath Bárdarbunga caldera, representing the magma reservoir; ii) a caldera ring fault system and iii) a dyke, which extends from the southeast edge of the caldera to the eruption site. We utilise a similar ring fault and magma reservoir geometry as employed by Gudmundsson et al. (2016). In addition we also incorporate the dyke geometry defined by Sigmundsson et al. (2015). We model the caldera ring fault, sill and dyke as a series of rectangular dislocations (patches) in an elastic half-space (Okada, 1992). We employ Bayes' Theorem to calculate the posterior probability distribution for slip on the ring fault and opening of the sill and dyke, assuming a uniform *a priori* probability over a range of possible values (Mosegaard and Tarantola, 1995;

Sigmundsson et al., 2015). We jointly solve for the opening along the dyke (24 patches in azimuth and 5 in depth), slip on each segment of the ring fault (24 patches in azimuth and 8 in depth) and the closing of the sill (85 patches).

Cumulative deformation modelling is carried out over six time periods (Table S2 in Supplementary Material) to determine the evolution of these multiple source parameters over the course of the eruption. To maximize the amount of input data used we undertook the modeling using a two-step process for the last three time periods (between 4th September 2014 to 10th April 2015) where cGPS /InSAR data was limited in the vicinity of the dyke from mid-September 2014 onwards. We ran separate cumulative deformation models for the periods 20140904-20141023, 20140904-20141218 and 20140904-20150410. Then summed the opening/slip derived from each of their median posterior distributions (for the ring fault, sill and dyke) to those computed for the 20140816-20140904 model, as this model incorporated the largest amount of input data for quality control purposes (see Table S2 in Supplementary Material).

Although an inflating dyke and deflating sill (or spherical source) have been incorporated in previous modelling studies (e.g. Sigmundsson et al., 2015, Riel et al., 2015, Green et al., 2015) these sources do not fully account for the near- and far-field deformation and/or agree with depth estimates of the melt, derived from petrological analysis (Gudmundsson et al., 2016). In order to satisfy these independent observations a large amount of fault slip is required at the caldera, combined with deflation of a reservoir at a depth below the caldera floor of between 8-12 km (Gudmundsson et al., 2016). We satisfy the above criteria by incorporating a reactivated ring fault system at the caldera, extending from 1 to 10 km, connected to a deflating sill at its base. Constraints on the geometry of the caldera fault system are described by Gudmundsson et al. (2016). During each time period analysed in this study (Table S2 in Supplementary Material) both dyke emplacement and caldera subsidence were occurring, so each model comprises all three components (ring fault, sill and dyke). The depth of the sill was here set to 10 km. This depth was determined from a probability density function (PDF) generated from one million iterations of a MCMC inversion of a point source (Mogi, 1958) in an elastic half-space, constrained by post-rifting cGPS and InSAR observations in the far-field (Gudmundsson et al., 2016). The peak of this PDF is at 10 km beneath the caldera floor with a 95% confidence interval of 8-12 km. Although the magma source must have a finite volume, which we model as a horizontal sill, a point source is a reasonable approximation for observations far away. The location and geometry of the upper edge of the caldera ring fault is determined from modelling a 1-day interferogram, which demonstrated good coherence on the ice-covered volcano, and coincided with three >M4, and a M5.3 earthquake which occurred on the 18^{th} September 2014, within the northern sector of the caldera. We assumed the fault on the northwest side dipped at 10 degrees to the northwest (Gudmundsson et al., 2016).

2.3 Stress modelling

We calculate the tensile and Coulomb failure stress change for each of the six time periods using our cumulative deformation models corresponding to each of these intervals. The stresses are calculated using a receiver fault orientation representative of the general orientation of the mapped surface and subsurface faults. Absolute stress state is difficult to attain, however, we compute based on seismic observations, the likely rake and planes of failure. Thus, our stress changes can be considered to either add or subtract from the absolute Coulomb stress. Given the strike (θ) and dip (δ) of a fault plane, the components of $\mathbf{v}$, the normal to that plane, are given by:

$$\nu_1 = \sin\delta \cos\theta \quad (1)$$

$$\nu_2 = \sin\delta \sin\theta \quad (2)$$

$$\nu_3 = \cos\delta \quad (3)$$

If the components of the stress tensor $\sigma_{ij,}$ represent the change in stress at each point on the fault, then the change in traction $\mathbf{\Delta T}$ on a fault with normal $\mathbf{\nu}$ is given by:

$$\Delta T_i = \Delta\sigma_{ij}\nu_j \quad (4)$$

The change in normal stress is then given by:

$$\Delta\sigma_n = \Delta T_i\nu_i \quad (5)$$

The magnitude of change in shear stress $\Delta\tau$ in the direction of a vector $\boldsymbol{\rho}$ in the plane of the fault is given by:

$$\Delta\tau = \Delta T_i\rho_i \quad (6)$$

The change in Coulomb stress $\Delta\sigma_c$ is then given by:

$$\Delta\sigma_c = \Delta\tau + \mu\,(\Delta\sigma_n - \frac{B}{3}\Delta\sigma_{kk}) \quad (7)$$

Where $\Delta\tau$ is the change in shear stress, μ is the coefficient of friction, $\Delta\sigma_n$ is the change in normal stress, B is the Skempton coefficient and $\Delta\sigma_{kk}$ is the volumetric stress change ($\Delta\sigma_{kk} = \Delta\sigma_{xx} + \Delta\sigma_{yy} + \Delta\sigma_{zz}$) (Cocco and Rice, 2002). We set $\mu = 0.6$ and B = 0.5 (after Árnadóttir et al., 2003). We calculate $\Delta\sigma_c$ in an elastic half-space and use a Poisson's ratio of 0.25 and a shear modulus of 30 GPa. We follow the convention that tensile stress is positive; therefore μ is also positive.

In accordance with the dip on most of the mapped subsurface faults defined by the relocated seismicity in the Tungnafellsjökull caldera, we assume that the receiver faults have a strike of 220 degrees and dip 55 degrees (to the west). This orientation agrees with the strike of most of the mapped subsurface faults, as well as the mapped surface faults/fractures within the Tungnafellsjökull fissure swarm (Björnsdóttir and Einarsson, 2013). This is also in general agreement with the strike of recent fault movements, observed in the field in the summer of 2015, along graben faults west and north of Tungnafellsjökull. To test the sensitivity of the results to variations in strike and dip, we ran a series of stress models assuming receiver faults with a strike of 230 degrees and dip of 90 degrees. We found that this did not significantly alter the final results, however predicts higher Coulomb stress changes in the northern part of the swarm where faults are closer to vertical.

3 Deformation and stress modeling results

Based on the analysis of geodetic and seismic data acquired throughout the unrest and eruption, the primary mechanism for the increased seismicity at Tungnafellsjökull may be evaluated. PS-InSAR analysis, spanning the entire period of unrest and eruption, displays no evidence of local deformation in the vicinity of Tungnafellsjökull volcano (Figure 3 and Figure S6 in Supplementary Material), while major deformation is observed within the Bárdarbunga volcanic system – related to both the slow caldera collapse and dyke emplacement. The lack of deformation at Tungnafellsjökull suggests that either no new intrusions/increase in pressure occurred here during the observation period, or the pressure changes related to any such event were too small to produce observable deformation at the surface. To determine the size of possible intrusions/increases in pressure within a resident chamber that may go undetected, a series of models were run using a Mogi point-source (Mogi, 1958) beneath Tungnafellsjökull for both a shallow and deeper magma chamber (depths of 2 and 7 km respectively, Figure S7 in Supplementary Material). These models suggest that any such intrusion or pressure increase within an existing reservoir within this depth range could not exceed a volume change of $\sim 4\times10^6$ m^3, which would produce one fringe (~1.5 cm) of deformation in the satellite's line-of-sight (LOS). This deformation is not observed on the PS-InSAR interferogram (Figure 3). We nevertheless consider these volumes maximum bounds, and determine whether the stress changes related to such an increase in volume could induce triggered seismicity at Tungnafellsjökull. Both tensile and Coulomb stress changes were calculated for a Mogi source at a depth of 7 km, since this model corresponds to a larger volume change and broader deformation signal. The results indicate that an inflationary source beneath Tungnafellsjökull could result in an increase in tensile/Coulomb stress here, however the area affected would be quite limited and would not account for the earthquake activity to the northeast or east of Tungnafellsjökull (Figure S8 in Supplementary Material). For these reasons, we consider a pressure increase under Tungnafellsjökull an unlikely cause for the earthquake activity. A deflation source beneath Tungnafellsjökull would have the opposite effect; clamping faults in the Tungnafellsjökull fissure swarm and reducing the likelihood of earthquakes (also Figure S8 in Supplementary Material).

Stress transfer may result from either small permanent static stress changes or larger transient dynamic changes (the latter of which is produced by the propagation of seismic waves). However, temporal correlation between the occurrences of large earthquakes at Bárdarbunga and earthquakes at Tungnafellsjökull is not observed (see section S9 in Supplementary Material). Many of the largest events do not induce almost instantaneous nucleation of earthquakes at Tungnafellsjökull, which would be expected to be the case for dynamic triggering, since the stress perturbation lasts a very short time. Furthermore, from Figure 2 we can see that the rate of seismicity went well above background levels before any large events occurred within the Bárdarbunga caldera and continued well above that level after the M5+ events had ceased. Therefore dynamic triggering of earthquakes at Tungnafellsjökull volcano is not the explanation for our observations.

In order to determine whether static stress changes associated with the 2014-2015 Bárdarbunga unrest and eruption could be responsible for the observed seismicity at Tungnafellsjökull, a robust model is required that is capable of reproducing both the near- and far-field deformation observed during this extended period. A series of optimal models were calculated for six time intervals throughout the unrest and eruption (Figure 2 and Table S2 in Supplementary Material). Each of the models incorporated a caldera ring fault system connected to a sill at its base (at a depth of 10 km) and a four-segment dyke extending from Bárdarbunga caldera to the eruption site. The optimal models derived for each of the intervals provides an excellent fit to the input data. An example of the results of the MCMC inversion to determine the optimal deformation model for the period 16th August – 4th September 2014 is displayed in Figure 4. A comparison between the data and the optimal models in displayed in Figure 4(a-f). Figure 4(g-i) display the median posterior probability of slip on the ring fault, closing of the sill and opening of the dyke respectively. By the end of August 2016 the dyke had reached it full length yet subsidence at the caldera amounted to ~0.5 m/day. This fast subsidence was related to magma withdrawal from the reservoir below, feeding the Holuhraun eruption where the effusion rate was high, 200-250 m^3/s in the first few weeks (Gudmundsson et al., 2016). Our model spanning

16th August to 4th September 2014 indicates that slip on the ring fault during this period (Figure 4g) averaged 16 m. The average closing of the sill was 19 m (Figure 4h), with larger amounts of closing observed in the eastern part of the sill. The average opening of the dyke was 1 m (Figure 4i), with greater opening towards the northeastern segments in the uppermost 4 km. The asymmetric closing of the sill is likely related to increased magma withdrawal from the eastern section. This pattern is consistent throughout the modelled time series and may be related to connectivity within the reservoir, or because of increased faulting in this region. The increased opening towards the end of the dyke is consistent with that observed by Sigmundsson et al. (2015) in the vicinity of the eruption site.

This model varies from that presented in Sigmundsson et al. (2015), in that it incorporates the caldera subsidence grid (from Gudmundsson et al., 2016) but more importantly a revised model geometry, comprising an enclosed caldera ring fault system connected to a sill at 10 km beneath Bárdarbunga. However the opening observed in the dyke is very similar to that presented by Sigmundsson et al. (2015). During the entire period analysed (20140816-20150410) our model indicates an average slip on the ring fault of 40 m, average closing of the sill of 50 m and average opening of the dyke of 1.5 m (Figure S10 in Supplementary Material).

The time series of slip multiplied by area (seismic potency) for the ring fault and volume change for the sill and dyke are displayed in Figure 5. The curves show an initial sharp increase in seismic potency until the 23rd October 2014, followed by a more gradual increase until the end of the eruption. The volume change curves for the sill and dyke appear to be more correlated. In general there is a significant increase in closing of the sill and opening of the dyke until the 13th September 2014, after which the volume changes become more gradual. However a smaller incremental closing of the sill between the 28th August-4th September 2014, appears to correlate to a larger incremental dyke opening during the same period. The final volume changes calculated up to the end date in the time series (10th April 2015) are -1.9 ± 0.1 km^3 for the deflation of sill, 8.2 ± 0.5 km^3 for the slip × area of the ring fault and 0.7 ± 0.04 km^3 for the inflation of the dyke (Figure 5). The volume change associated with the deflation of the sill agrees with estimates of the collapse volumes calculated by Gudmundsson et al (2016) (1.8 ± 0.2 km^3). The volume intruded into the dyke for the model ending on the 4th September 2014 (0.6 km^3), is larger than that presented in Sigmundsson et al. (2015). This is due to the different caldera model being used, leading to more opening at the corner of the second dyke segment (Figure 4i). This was corrected for by replacing the patches in this column with the median value of those in the adjacent column. The calculated final volume on the 4th September 2014, using this corrected corner opening is 0.5 km^3 – the same as that determined by Sigmundsson et al. (2015). At the end of the eruption the final corrected volume for the dyke is 0.6 km^3, suggesting that some continued widening/post-rifting inflation of the dyke did occur during this period.

To assess the effect of the caldera collapse and dyke emplacement in terms of its potential to modify the existing stress field, we calculated the stress changes resulting from the modelled deformation sources within the Bárdarbunga magmatic system. This was undertaken for the same six time periods (spanning the entirety of the unrest and eruption), utilised in the deformation modelling (Figure 2 and Table S2 in Supplementary Material). The time series of Coulomb stress changes from the 16th August 2014 until the 10th April 2015, for the 0-4 km depth interval, are displayed in Figure 6 (this interval contained the largest number of earthquakes). The tensile stress changes are displayed in Figure S11 (Supplementary Material) along with the

Coulomb and tensile stress changes for the 4-8 km interval (Figures S12 and S13 in Supplementary Material). The stress field below this depth is not considered, due to the fact that the majority of the relocated events are at depths shallower than 9 km and the observation that the deeper events more commonly occurr during periods of absence of data from the closest seismic station (at Vonarskard), making these source depths less reliable. In each of these figures tensile stress is positive.

The time series of Coulomb stress changes for the depth interval 0-4 km, shows an initial an increase in Coulomb stress trending from Bárdarbunga towards the northeastern edge of both Tungnafellsjökull and Vonarskard – the magnitude of which increases throughout the observation period (Figure 6). Earthquakes initially occur in zones of elevated Coulomb stress <0.05 MPa within the Vonarskard caldera and on the northeastern edge of Tungnafellsjökull. Maximum Coulomb stress changes in the vicinity of Tungnafellsjökull are reached by 18th December 2014 (~0.25 MPa). The tensile stress changes display a similar trend of increased stress towards the northeast of Tungnafellsjökull and Vonarskard (Figure S11 in Supplementary Material), with broader regions of increased stress observed after the 4th September 2014. These areas tend to be slightly more localised than the Coulomb stress changes, but still encapsulate the majority of the earthquakes.

The Coulomb stress changes for the deeper interval (4-8 km, Figure S12 in Supplementary Material) display a more complex evolution through time than the 0-4 km interval, but with the largest increases in Coulomb stress still observed at Tungnafellsjökull and Vonarskard after 4th September 2014. The tensile stress changes at this interval display a similar trend including an apparent reduction in stress in the vicinity of both Tungnafellsjökull and Vonarskard during the 28th August-4th September 2014 (Figure S13b in Supplementary Material). In general, the calculated stress changes (both normal and Coulomb) for these two depth intervals are in good agreement with both the spatial and temporal variation in seismicity, indicating that earthquakes are occurring in regions of increased tensile and Coulomb stress.

To determine the dominant source influence of these observed variations in normal and Coulomb stress, the calculations were rerun for the deformation model spanning the 16th August 2014 to the 10th April 2015, using model components which contribute to the observed deformation field separately (e.g. a separate calculation was undertaken for i) slip on the ring fault and closing of the sill and ii) opening of the dyke. The results are displayed in Figure S14 (Supplementary Material), and demonstrate that the closing of the sill/slip on the ring fault system is the primary cause of the large positive stress changes observed in the vicinity of Tungnafellsjökull, whereas the dyke influences the stress changes in this region by reducing the tensile and Coulomb stress in the northeast sector of Tungnafellsjökull. This suggests the stress changes observed in this area result from a complex interaction between those induced by the deflating magma reservoir/caldera collapse and the emplacement of a long dyke. This interplay is likely the result of the apparent reduction in stress observed between the 28th August-4th September, as during this period the modeling indicates a small incremental closure of the sill but a larger opening of the dyke.

4 Discussion

We present a compelling example of how a major slow caldera collapse and associated dyke intrusion triggered seismicity within the fissure swarm of a neighbouring volcanic system, some 25 km away. Earthquakes occurred in regions of positive changes in tensile and Coulomb stress over a series of depth and time intervals. The region of positive changes in tensile and Coulomb stress extend over a wide area from the Bardarbunga caldera to Tungnafellsjökull. However, the triggered earthquake activity is mostly confined to a part of the Tungnafellsjökull fissure swarm. The tensile and Coulomb stress changes in this area are between <0.05-0.25 MPa. Our interpretation is that faults in this area were previously close to failure, and accordingly, unclamping of faults within the Tungnafellsjökull central volcano are responsible for the observed increase in seismicity rates in this area. Although stress changes related to a hypothetical undetected intrusion/inflation event directly beneath Tungnafellsjökull could produce a similar magnitude stress change, the region of increased tensile/Coulomb would be restricted to a small area (Figure S8 in Supplementary Material), and this would not account for the spatial distribution of relocated earthquakes that occurred throughout this event. Therefore we consider it unlikely.

Understanding volcano triggering effects is important for evaluation of volcanic hazards. Modelling such as that presented here, can directly help evaluate hazards during an eruption and thus facilitate effective eruption response. In addition to the activity at Tungnafellsjökull, it was unclear if small clusters of earthquakes, occurring within the Vonarskard caldera, between Tungnafellsjökull and Bárdarbunga (Figure 1c) were related to a local intrusion. The stress modelling results show that these earthquakes coincide with a lobe of elevated positive stress changes (Figures 6 and S11), suggesting that they were the result of unclamping and movement on pre-existing faults – primarily triggered by the magma withdrawal and subsidence at the neighbouring Bárdarbunga volcano.

Our results can be compared to triggering studies at other volcanoes. Both stress changes (e.g., Lind & Sacks 1998; Rowland et al., 2010; Palladino and Sottili; 2012), and hydraulic connections such as a dyke intrusion intersecting a magma reservoir beneath a neighbouring volcano, tapping of multiple reservoirs, and pore pressure diffusion within the asthenosphere (e.g., Hildreth, 1991; Eichelberger and Izbekov, 2000; Ebinger et al., 2008, Gonnermann et al., 2012) have frequently been attributed as the cause of coupled activity. In Iceland, the only other closely spaced volcano pair studied for triggering effects are the Eyjafjallajökull and Katla volcanoes in South Iceland. These reside at a similar distance from each other as Bárdarbunga and Tungnafellsjökull. In that case, intrusive and eruptive activity at Eyjafjallajökull is inferred to have had minor influence on the magmatic system of Katla (Albino and Sigmundsson, 2014). Magma moving in the roots of the Eyjafjallajökull volcano was an order of magnitude less than at Bárdarbunga, explaining the lack of triggering effects.

A case of lateral dyke intrusion from one volcano intersecting a magma body within the domain of another volcano is inferred to be the cause of the 1996 Gjálp eruption in Iceland. There, geochemical and seismic data suggest that a dyke propagated from Bárdarbunga and intersected a magma body in the domain of the nearby Grimsvötn central volcano, located midway between the two volcanoes (Pagli et al., 2007). The erupted material has an isotopic signature comparable to that of eruptive products of the Grimsvötn volcano (Sigmarsson et al., 2000). There is no evidence that a dyke propagated from Bárdarbungna to Tungnafellsjökull during the recent eruption.

Gonnermann et al. (2012) modelled recent contemporaneous uplift at neighbouring Kilaeua and Mauna Loa volcanoes (a few tens of kilometers apart), via pore pressure diffusion within an asthenospheric layer of melt accumulation. Although the combined uplift could be accounted for using this model, the authors also noted that the heightened intrusive/eruptive activity at Kilauea during this period likely inhibited an eruption at Mauna Loa. The deformation pattern during episodes of unrest at a series of volcanoes residing within the Kenyan Rift were examined by Biggs et al. (2016). In the northern part of the Kenyan Rift, Paka volcano displayed variable deformation between 2006-2010 related to the inflation/deflation of four distinct sources. During the same time interval neighbouring Silali volcano (less than 25 km away) displayed a continued long-term subsidence (1-2 cm/yr), likely related to cooling/crystallisation of a shallow magma chamber. In the southern part of the Kenyan Rift, Logonot volcano exhibited a phase of rapid uplift between 2004-2006, followed by a period of gradual subsidence (2007-2010). However, nearby volcanoes Olkaria and Suswa (15 and 30 km away respectively from Logonot) showed no indication of deformation during this period. The authors suggest that for small increases in melt supply (causing unrest), interaction is limited to magma sources <10 km apart. Tungnafellsjökull and Bárdarbunga are ~25 km apart and reside within separate, distinct fissure swarms. The lack of any observed GPS or InSAR deformation of local origin at or near Tungnafellsjökull volcano, during this major eruption within the Bárdarbunga system, indicates that the two subsurface plumbing systems are not connected. There is no evidence of a decrease in pressure beneath Tungnafellsjökull, which would be indicative of either pore pressure diffusion or magma tapping – so no evidence for a hydraulic connection between the volcanoes. However, rapid stress changes associated with major eruptions (10^9-10^{11} km^3), may trigger activity >25 km away. In this case, the stress changes can cause simultaneous eruptions e.g. at Suswa and Longonot volcanoes in the Keyan Rift (Scott and Skilling,

1999) and Rotorua and Ohakuri calderas in New Zealand (Bégué et al, 2014). Both of these examples were major caldera forming eruptions. The synchronous caldera collapse between Suswa and Logonot is thought to have resulted from lateral magma movement along rift floor tension fractures combined with decompression of shallow reservoirs. Bégué, et al. (2014) proposed that the 240 ka simultaneous eruption of over 245 km^3 of rhyolitic magma from Rotorua and Ohakuri calderas (30 km apart) is linked to the existence of a continuous intermediate mush zone beneath the region, comprising isolated batches of magma. Stress perturbations rather than magma recharge has been suggested by the authors as the triggering mechanism for this super eruption – with the evacuation of an initial batch of magma leading to the activation of regionally linked faults, triggering the eruption of juxtaposed melt lenses within the mush layer.

Our geodetic and seismic data are consistent with triggered seismicity on faults in the Tungnafellsjökull fissure swarm. Faults in these areas were inspected in summers of 2015 and 2016, and the primary observation is that a number of them showed fresh sinkholes, with some evolution between years. Fresh sinkholes identified in the summer of 2016 indicate that the movements appear to be continuing following the end of the eruption. The sinkholes were all associated with faults, and yet not all faults showed fresh sinkholes. This supports the conclusion that the fresh sinkholes are due to fault movements on the faults that show them. The associated fault displacements are inferred to be small (less than several centimetres) since they were not detected on InSAR – but the overlying sediment cover of fissures may widen considerably, forming localised sinks when the surface sediments trickle into them, possibly facilitated by precipitation or the summer melting of the winter snow.

This is not the first time that triggered activity has been observed within the Tungnafellsjökull's fissure swarm. During the 1996 Gjálp subglacial eruption (20 km south of Bárdarbunga) and associated unrest at Bárdarbunga, Pagli et al. (2007) identified three linear deformation signals, less than four km long, to the northwest, north and northeast of Tungnafellsjökull volcano using a series of co-eruptive interferograms. A sharp lineation to the north was the most prominent, corresponding to ~14 mm of motion in the satellite's LOS. The authors determined that the deformation observed to the north of Tungnafellsjökull was consistent with either a slipping fault or a dyke injection, however, fault slip was considered the most likely mechanism since no deformation was observed at Tungnafellsjökull. Björnsdóttir and Einarsson (2013) also reported earlier fault movements (sinkholes) within the Tungnafellsjökull fissure swarm, as recent as 2010, in the same areas as fault movements mapped using InSAR during the 1996 Gjálp eruption (Pagli et al., 2007). The abnormally high ratio of geodetic moment to seismic moment during 1996-2010 suggested to Björnsdóttir and Einarsson (2013) that there might have been a magmatic component to these events, following the argumentation of Pedersen et al. (2007). The moment ratio was however, within the normal range for the recent events. The observed surface effects of triggered activity in the Tungnafellsjökull fissure swarm, in relation to both the 1996 and 2014-2015 eruptions, are consistent with our conclusion that faults in this area are close to failure and thus produce triggered seismicity when subject to positive changes in tensile and Coulomb stress.

Conclusions

Between the 16th August 20140 – 27th February 2015, ~1.9 km^3 of magma was withdrawn from a chamber beneath the Bárdarbunga central volcano and transferred through a 48 km long dyke, that in turn fed a fissure eruption at the Holuhraun plain. Our modelling results demonstrate that the combination of magma withdrawal from a reservoir at 10 km beneath Bárdarbunga, reactivation of the caldera ring fault system and inflation of a segmented dyke can reproduce the entire deformation field (both near- and far-field) observed during the 2014-2015 eruption. The total volume changes calculated during the deformation modelling are -1.9 ± 0.1 km^3 for the deflation of sill, 8.2 ± 0.5 km^3 for the slip × area (seismic potency) of the ring fault and 0.6 ± 0.04 km^3 for the inflation of the dyke (corrected volume). The computed volume change in the dyke up until the 4th September 2015 is 0.5 km^3. However, our dyke volume after the end of the eruption is 0.1 km^3 greater, indicating some continued widening during the eruption or post-rifting inflation of the dyke. Our computed volume change associated with the deflation of the sill is comparable to the total combined volume of magma intruded into the dyke (0.6 ± 0.04 km^3, from this study) and the volume of erupted lava (1.4 ± 0.2 km^3, Gudmundsson et al., 2016).

The excellent spatial and temporal correlation between regions of unclamping/increased Coulomb stress and relocated earthquakes, and the predominant normal mechanisms, combined with the absence of detectable deformation in the vicinity of Tungnafellsjökull, is indicative that the increased earthquake activity observed at this volcano was triggered by the recent unrest and eruption within the Bárdarbunga volcanic system. The cumulative seismicity plot also corroborates this, as the onset of increased seismicity rate coincides with the start of the caldera collapse (20th August 2014) and flattens off near the end of the eruption, when caldera subsidence rates were minimal. This strongly suggests that the primary effect causing the seismicity must be stress changes due to the caldera subsidence.

Acknowledgements

We thank two anonymous reviewers for their constructive comments. This research was funded through the European Community's Seventh Framework Programme Grant No. 308377 (Project FUTUREVOLC) and the NASA Earth and Space Science Fellowship (NESSF). We gratefully acknowledge FUTUREVOLC partners for their collaboration. COSMO-SkyMed data were provided by the Italian Space Agency (ASI) and TerraSAR-X data were provided by the German Aerospace Center (DLR), both through the Icelandic Volcanoes Supersite project, supported by the Committee on Earth Observing Satellites (CEOS). An intermediate TanDEM-X digital elevation model was provided by DLR under project IDEM_GEOL0123. Eyjólfur Magnusson generated the merged DEM used in the InSAR processing. The South Iceland Lowland (SIL) network monitoring team at the Icelandic Meteorological Office provided the seismic data used in this study. The subsidence of Bárdarbunga was mapped by the surveying aircraft of Isavia (Icelandic Aviation Operation Services) and from satellite images acquired by Pléiades (Centre National d'Études Spatiales (CNES) CNES 2014, Distributed Airbus DS, subsidised access provided by the French Space Agency CNES's ISIS program) and SPOT 6 (Airbus DS 2014).

References

Albino, F., & Sigmundsson, F. (2014). Stress transfer between magma bodies: influence of intrusions prior to 2010 eruptions at Eyjafjallajökull volcano, Iceland. *Journal of Geophysical Research: Solid Earth*, *119*(4), 2964-2975.

Árnadóttir, T., Jónsson, S., Pedersen, R., & Gudmundsson, G. B. (2003). Coulomb stress changes in the South Iceland Seismic Zone due to two large earthquakes in June 2000. *Geophysical Research Letters*, *30*(5).

Bégué, F., Deering, C. D., Gravley, D. M., Kennedy, B. M., Chambefort, I., Gualda, G. A. R., & Bachmann, O. (2014). Extraction, storage and eruption of multiple isolated magma batches in the paired Mamaku and Ohakuri eruption, Taupo Volcanic Zone, New Zealand. *Journal of Petrology*, *55*(8), 1653-1684.

Biggs, J., Robertson, E., & Cashman, K. (2016). The lateral extent of volcanic interactions during unrest and eruption. *Nature Geoscience*.

Björnsdóttir, T., & Einarsson, P. (2013). Evidence of recent fault movements in the Tungnafellsjökull fissure swarm in the Central Volcanic Zone, Iceland. *Jökull*, *63*, 17-32.

Böðvarsson, R., S. Th. Rögnvaldsson, S. S. Jakobsdóttir, R. Slunga and R. Stefánsson (1996). The SIL Data Acquisition ans Monitoring System. *Seism. Res. Lett., 67*, 5, 35-46.

Böðvarsson, R., S.Th. Rögnvaldsson, R. Slunga and E. Kjartansson (1999). The SIL data acquisition system – at present and beyond year 2000. *Phys. Earth Plan. Int. 113*, 89–101.

Cocco, M., & Rice, J. R. (2002). Pore pressure and poroelasticity effects in Coulomb stress analysis of earthquake interactions. *Journal of Geophysical Research: Solid Earth*, *107*(B2).

Diez, M., La Femina, P. C., Connor, C. B., Strauch, W., & Tenorio, V. (2005). Evidence for static stress changes triggering the 1999 eruption of Cerro Negro Volcano, Nicaragua and regional aftershock sequences. *Geophysical research letters*, *32*(4).

Ebinger, C. J., Keir, D., Ayele, A., Calais, E., Wright, T. J., Belachew, M., ... & Buck, W. R. (2008). Capturing magma intrusion and faulting processes during continental rupture: seismicity of the Dabbahu (Afar) rift. *Geophysical Journal International*, *174*(3), 1138-1152.

Eichelberger, J. C., & Izbekov, P. E. (2000). Eruption of andesite triggered by dyke injection: contrasting cases at Karymsky Volcano, Kamchatka and Mt Katmai, Alaska. *Philosophical Transactions of the Royal Society of London A: Mathematical, Physical and Engineering Sciences*, *358*(1770), 1465-1485.

Einarsson, P., & Saemundsson, K. (1987). *Earthquake Epicenters 1982-1985 and Volcanic Systems in Iceland: Upptök jardskjalfta 1982-1985 og eldstodvakerfi á Íslandi*. Menningarsjodur.

Einarsson, P. (2015). The Tungnafellsjökull volcanic system. In: Ilyinskaya, Larsen and (eds.): *Catalogue of Icelandic Volcanoes.* IMO, UI, CPD-NCIP.

Freed, A. M. (2005). Earthquake triggering by static, dynamic, and postseismic stress transfer. *Annu. Rev. Earth Planet. Sci.*, *33*, 335-367.

Gonnermann, H. M., Foster, J. H., Poland, M., Wolfe, C. J., Brooks, B. A., & Miklius, A. (2012). Coupling at Mauna Loa and Kilauea by stress transfer in an asthenospheric melt layer. *Nature Geoscience*, *5*(11), 826-829.

Green, R. G., Greenfield, T., & White, R. S. (2015). Triggered earthquakes suppressed by an evolving stress shadow from a propagating dyke. *Nature Geoscience*, *8*(8), 629-632.

Gudmundsson, M.T., Jónsdóttir, K., Hooper, A., Holohan, E.P., Halldórsson, S.A., Ófeigsson, B.G., Cesca, S., Vogfjörd, K.S., Sigmundsson, F., Högnadóttir, T., Einarsson, P., Sigmarsson, O., Jarosch, A.H., Jónasson, K., Magnússon, E., Hreinsdóttir, S., Bagnardi, M., Parks, M.M., Hjörleifsdóttir, V., Pálsson, F., Walter, T.R., Schöpfer, M.P.J., Heimann, S., Reynolds, H.I., Dumont, S., Bali, E., Gudfinnsson, G.H., Dahm, T., Roberts, M.J., Hensch, M., Belart, J.M.C., Spaans, K., Jakobsson, S., Gudmundsson, G.B., Fridriksdóttir, H.M., Drouin, V., Dürig, T., Aðalgeirsdóttir, G., Riishuus, M.S., Pedersen, G.B.M., van Boeckel, T., Oddsson, B., Pfeffer, M.A., Barsotti, S., Bergsson, B., Donovan, A., Burton, M.R. and Aiuppa, A. (2016). Gradual caldera collapse at Bárdarbunga volcano, Iceland, regulated by lateral magma outflow. *Science*, *353*(6296), aaf8988.

Harris, R. A., & Simpson, R. W. (1992). Changes in static stress on southern California faults after the 1992 Landers earthquake. *Nature*, *360*, 251-254.

Heimisson, E. R., Einarsson, P., Sigmundsson, F., & Brandsdóttir, B. (2015). Kilometer-scale Kaiser effect identified in Krafla volcano, Iceland. *Geophysical Research Letters*, *42*(19), 7958-7965.

Hildreth, W. (1991). The timing of caldera collapse at Mount Katmai in response to magma withdrawal toward Novarupta. *Geophysical Research Letters*, *18*(8), 1541-1544.

Hill, D., F. Pollitz, C. Newhall, Earthquake–volcano interactions, *Phys. Today, 55* (11) (2002), pp. 41–47.

Hjartardóttir, Á. R., Einarsson, P., Gudmundsson, M. T., & Högnadóttir, T. (2016). Fracture movements and graben subsidence during the 2014 Bárðarbunga dike intrusion in Iceland. *Journal of Volcanology and Geothermal Research*, *310*, 242-252.

Icelandic Met Office. (2016). *Earthquakes.* Available: http://en.vedur.is/earthquakes-and-volcanism/earthquakes. Last accessed 12th Aug 2016.

Jónsson, S. (2009). Stress interaction between magma accumulation and trapdoor faulting on Sierra Negra volcano, Galápagos. *Tectonophysics*, *471*(1), 36-44.

King, G. C., Stein, R. S., & Lin, J. (1994). Static stress changes and the triggering of earthquakes. *Bulletin of the Seismological Society of America*, *84*(3), 935-953.

La Femina, P.C., C.B. Connor, B.E. Hill, W. Strauch, J.A. Saballos, Magma-tectonic interactions in Nicaragua: the 1999 seismic swarm and eruption of Cerro Negro volcano, *J. Volcanol. Geotherm. Res., 137* (2004), pp. 187–199.

Larsen, G. and Gudmundsson, M.T., 2015. The Bárdarbunga volcanic system. In: Ilyinskaya, Larsen and Gudmundsson (eds.): *Catalogue of Icelandic Volcanoes.* IMO, UI, CPD-NCIP.

Linde, A. T., & Sacks, I. S. (1998). Triggering of volcanic eruptions. *Nature*, *395*(6705), 888-890.

Manga, M., & Brodsky, E. (2006). Seismic triggering of eruptions in the far field: volcanoes and geysers. *Annu. Rev. Earth Planet. Sci*, *34*, 263-291.

Marzocchi, W., Casarotti, E., & Piersanti, A. (2002). Modelling the stress variations induced by great earthquakes on the largest volcanic eruptions of the 20th century. *Journal of Geophysical Research: Solid Earth*, *107*(B11).

Mogi, K. (1958), Relations between the eruptions of various volcanoes and the deformations of the ground sources around them. *Bulletin of the Earthquake Research Institute, 36*, 99–134.

Mosegaard, K., & Tarantola, A. (1995). Monte Carlo sampling of solutions to inverse problems. *Journal of Geophysical Research: Solid Earth*, *100*(B7), 12431-12447.

Nostro, C., Stein, R.S., Cocco, M., Belardinelli, M.E., Marzocchi, W., 1998. Two-way coupling between Vesuvius eruptions and southern Apennine earthquakes, Italy, by elastic stress transfer. *J. Geophys. Res. 103*, 24,487 - 24, 504.

Okada, Y. (1992). Internal deformation due to shear and tensile faults in a half-space. *Bulletin of the Seismological Society of America*, *82*(2), 1018-1040.

Pagli, C., Sigmundsson, F., Pedersen, R., Einarsson, P., Árnadóttir, T., & Feigl, K. L. (2007). Crustal deformation associated with the 1996 Gjálp subglacial eruption, Iceland: InSAR studies in affected areas adjacent to the Vatnajökull ice cap. *Earth and Planetary Science Letters*, *259*(1), 24-33.

Palladino, D. M., & Sottili, G. (2012). On the space-time distribution of major explosive volcanic eruptions on Earth. *Geophysical Research Letters*, *39*(12).

Parsons, T., Thompson, G.A., Cogbill, A.H., 2006. Earthquake and volcano clustering via stress transfer at Yucca Mountain, Nevada. *Geology 34*, 785–788.

Pedersen, R., F. Sigmundsson, P. Einarsson (2007) Controlling factors on earthquake swarms associated with magmatic intrusions; constraints from Iceland. *J. Volcanol. Geothermal Res., 162*, 73-80. doi:10.1016/j.jvolgeores.2006.12.010.

Riel, B., Milillo, P., Simons, M., Lundgren, P., Kanamori, H., & Samsonov, S. (2015). The collapse of Bárdarbunga caldera, Iceland. *Geophysical Journal International*, *202*(1), 446-453.

Roman, D. C., & Heron, P. (2007). Effect of regional tectonic setting on local fault response to episodes of volcanic activity. *Geophysical research letters*, *34*(13).

Rowland, J. V., Wilson, C. J., & Gravley, D. M. (2010). Spatial and temporal variations in magma-assisted rifting, Taupo Volcanic Zone, New Zealand. *Journal of Volcanology and Geothermal Research*, *190*(1), 89-108.

Scott, S. C., & Skilling, I. P. (1999). The role of tephrachronology in recognizing synchronous caldera-forming events at the Quaternary volcanoes Longonot and Suswa, south Kenya Rift. *Geological Society, London, Special Publications*, *161*(1), 47-67.

Sigmarsson, O., Karlsson, H.R., Larsen, G., 2000. The 1996 and 1998 subglacial eruptions beneath the Vatnajökull ice sheet in Iceland: contrasting geochemical and geophysical inferences on magma migration. *Bull. Volcanol. 61*, 468–476.

Sigmundsson, F., Hooper, A., Hreinsdóttir, S., Vogfjörd, K. S., Ófeigsson, B. G., Heimisson, E. R., Dumont, S., Parks, M., Spaans, K., Gudmundsson, G. B., Drouin, V., Árnadóttir, T., Jónsdóttir, K., Gudmundsson, M. T., Högnadóttir, T., Fridriksdóttir, H. M., Hensch, M., Einarsson, P., Magnússon, E., Samsonov, S., Brandsdóttir, B., White, R., Ágústsdóttir, T., Greenfield, T., Green, R. G. et al.

(2015). Segmented lateral dyke growth in a rifting event at Bárðarbunga volcanic system, Iceland. *Nature*. 517, 191–195, doi:10.1038/nature14111 (Online 15 December 2014).

Slunga, R., Rögnvaldsson, S.Th. and Bödvarsson, R. (1995). Absolute and relative locations of similar events with application to microearthquakes in southern Iceland. *Geophys. J.Int. 123*, 409-419.

Stefánsson, R., R. Böðvarsson, R. Slunga, P. Einarsson, S. Jakobsdóttir, H. Bungum, S. Gregersen, J. Havskov, J. Hjelme, and H. Korhonen,. Earthquake prediction research in the South Iceland seismic zone and the SIL project (1993). *Bull. Seismol. Soc. Am. 83*, 696-716.

Stein, R. S., King, G. C., & Lin, J. (1992). Change in failure stress on the southern San Andreas fault system caused by the 1992 magnitude= 7.4 Landers earthquake. *Science, 258*(5086), 1328-1332.

Stein, R. S. (1999). The role of stress transfer in earthquake occurrence. *Nature*, *402*(6762), 605-609.

Toda, S., Stein, R. S., Richards-Dinger, K., & Bozkurt, S. B. (2005). Forecasting the evolution of seismicity in southern California: Animations built on earthquake stress transfer. *Journal of Geophysical Research: Solid Earth*, *110*(B5).

Walter, T. R., & Amelung, F. (2007). Volcanic eruptions following M≥ 9 megathrust earthquakes: Implications for the Sumatra-Andaman volcanoes. *Geology*, *35*(6), 539-542.

Figures

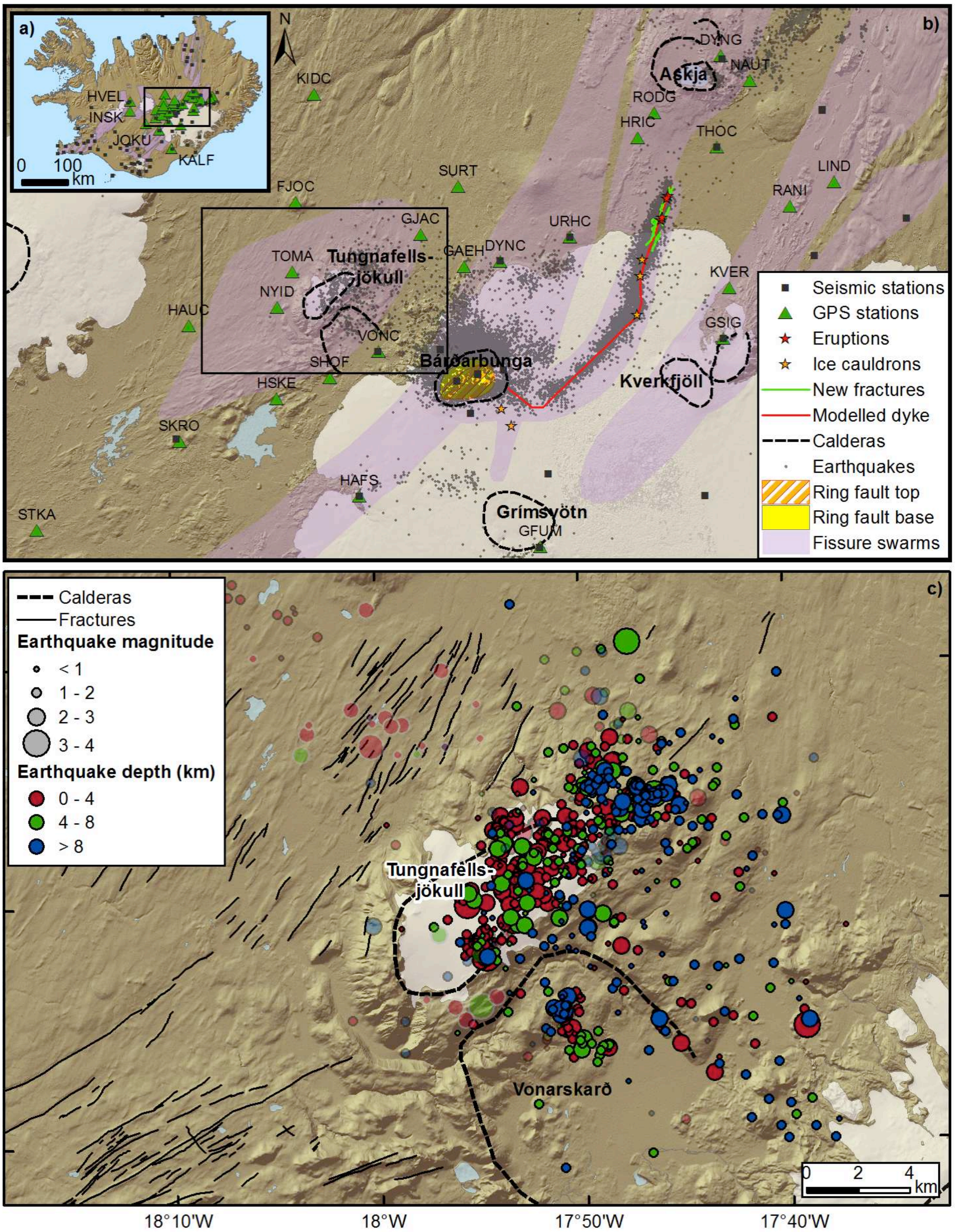

Figure 1. Location map. a) Map of Iceland displaying fissure swarms from Einarsson and Sæmundsson (1987), outline of study area (black box) and data utilised in this study. b) The Bárdarbunga and Tungnafellsjökull volcanoes. Earthquakes epicenters from 15 August 2014-10 April 2015 (Icelandic Met Office, 2016) are displayed along with eruptive sites and the location of the modelled ring fault, sill and dyke. c) Relocated earthquakes that occurred in the vicinity of Tungnafellsjökull during the period 5th October 1996 – 8th March 2015. Opaque earthquakes displayed with black outlines occurred between 15th August 2014 and 8th March 2015. Transparent earthquakes with black outlines occurred between 12th April 1998 – 14th August 2014. Those with light-grey outlines occurred between 5th of October 1996 and 11th April

1998. During this period there is larger error in the hypocenter locations due to gaps in the seismic network. Mapped surface fractures are from Björnsdóttir and Einarsson (2013). The intermediate TanDEM-X digital elevation model provided by DLR is displayed in the background of figures b and c.

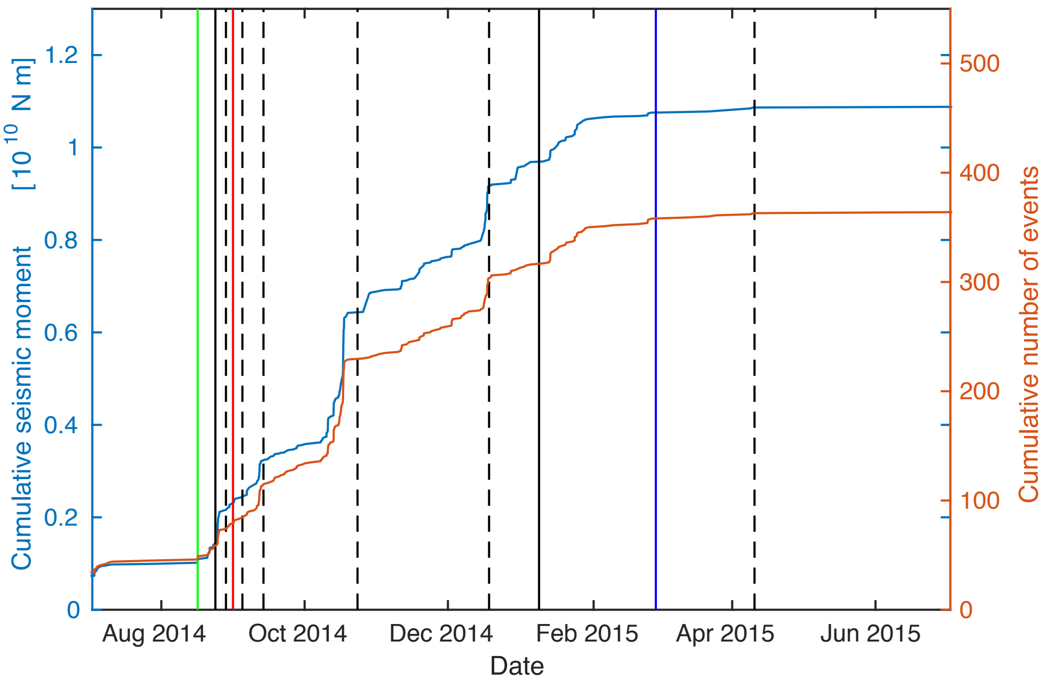

Figure 2. Cumulative number of earthquakes/seismic moment at Tungnafellsjökull since mid 2014. The vertical green line marks the start of unrest on the 16th August 2014, the vertical red line the start of the main eruption (31st August 2014) and the vertical blue line the end of the eruption on the 27th February 2015. The solid black lines indicate the first and last of the >M5 earthquakes which occurred within Bárdarbunga caldera. The black dashed lines indicate the end dates for each of the six time periods modelled. The figure shows that much of the activity occurred in swarms of a few days duration. The region used corresponds to the black box displayed in Figure 1b. Earthquakes are filtered by the magnitude of completeness (Mc) 1.5, to remove any artifacts caused by changes in network sensitivity. The zero reference for the y-axis is the beginning of 2010.

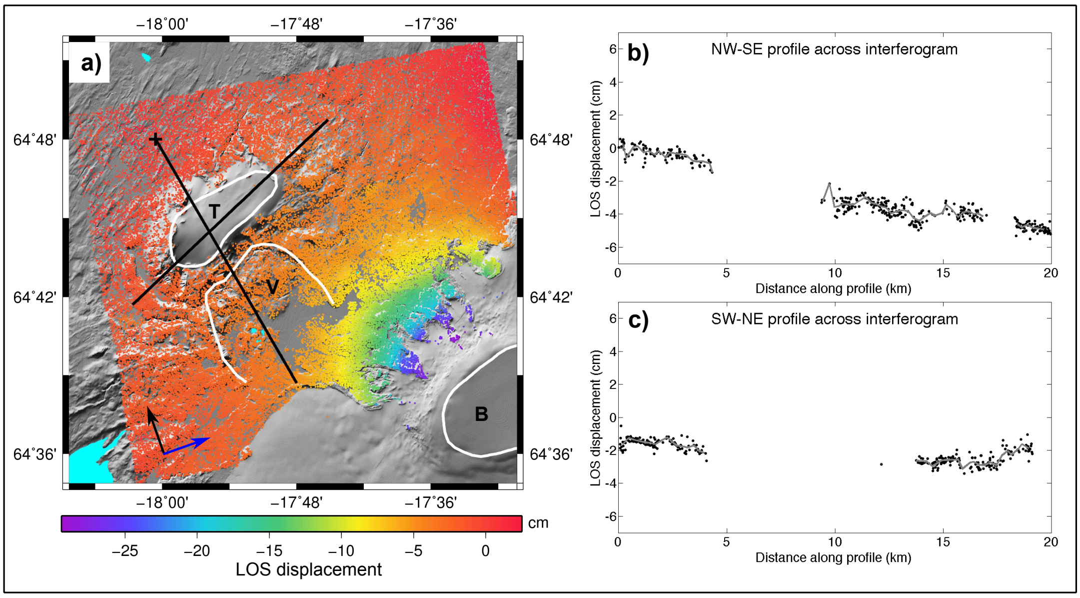

Figure 3. PS-InSAR analysis at Tungnafellsjökull. a) PS-InSAR cumulative line-of-sight (LOS) deformation map for the period 28th August 2014 to 29th July 2015, for ascending COSMO-SkyMed (CSK) SAR data. Underlying relief grid is the intermediate TanDEM-X DEM. Caldera outlines for Tungnafellsjökull (T), Vonarskard (V) and Bárdarbunga (B) are displayed in white. Satellite heading and look direction are displayed as black and blue arrows respectively. LOS displacements are positive towards the satellite. The reference point is displayed as a black cross. The movement away from the satellite (e.g. blue and purple amplitudes) displayed northwest of Bárdarbunga results from magma withdrawal beneath Bárdarbunga during the 2014-2015 eruption. b) Northwest-southeast profile across interferogram displayed in a). c) Southwest-northeast profile across interferogram displayed in a). In both b) & c) black dots represent individual PS-InSAR points extracted along profiles and solid grey line is the average LOS displacement.

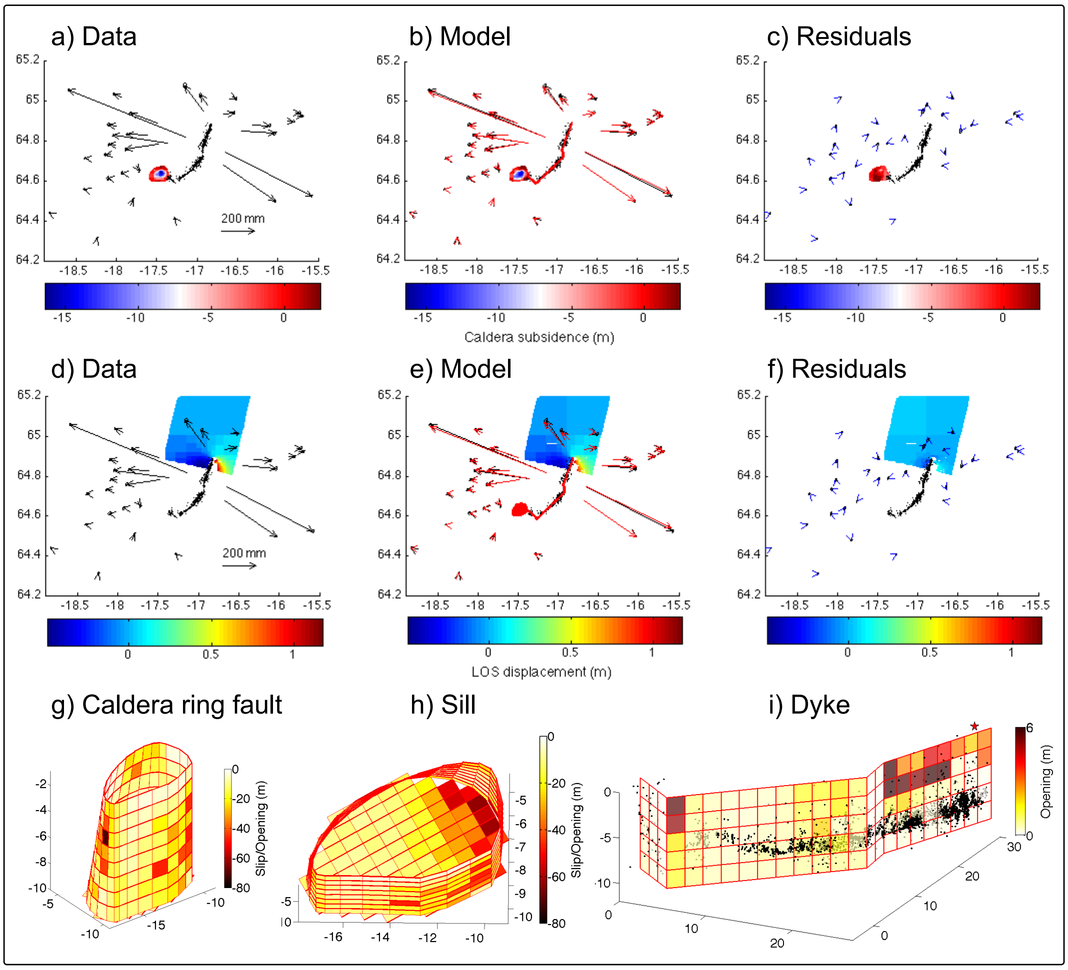

Figure 4. Cumulative deformation model computed in this study, for the period 16th Aug – 4th Sep 2014. Figures a-f display input data (a & d), optimal models (b & e) and residuals (c & f). In figures (a-f), cGPS vectors are displayed with black arrows, modeled vectors in red and residuals in blue. In (a-c) the colour scale represents the cumulative caldera subsidence from the 16th August 2014 – 5th September 2014. In (d-f) the colour scale represents the line-of-sight displacement (LOS) derived from a descending TSX interferogram covering the period 2nd August 2014 – 3rd September 2014. LOS displacement is positive towards the satellite. Figures (g-i) show the calculated median posterior slip on the ring fault (looking towards the northeast) (g), closing of the sill (looking towards the northeast) (h) and opening of the dyke (looking northwest) (i). Negative slip in (g) represents downward displacement and negative opening in (h) represents closing of the sill.

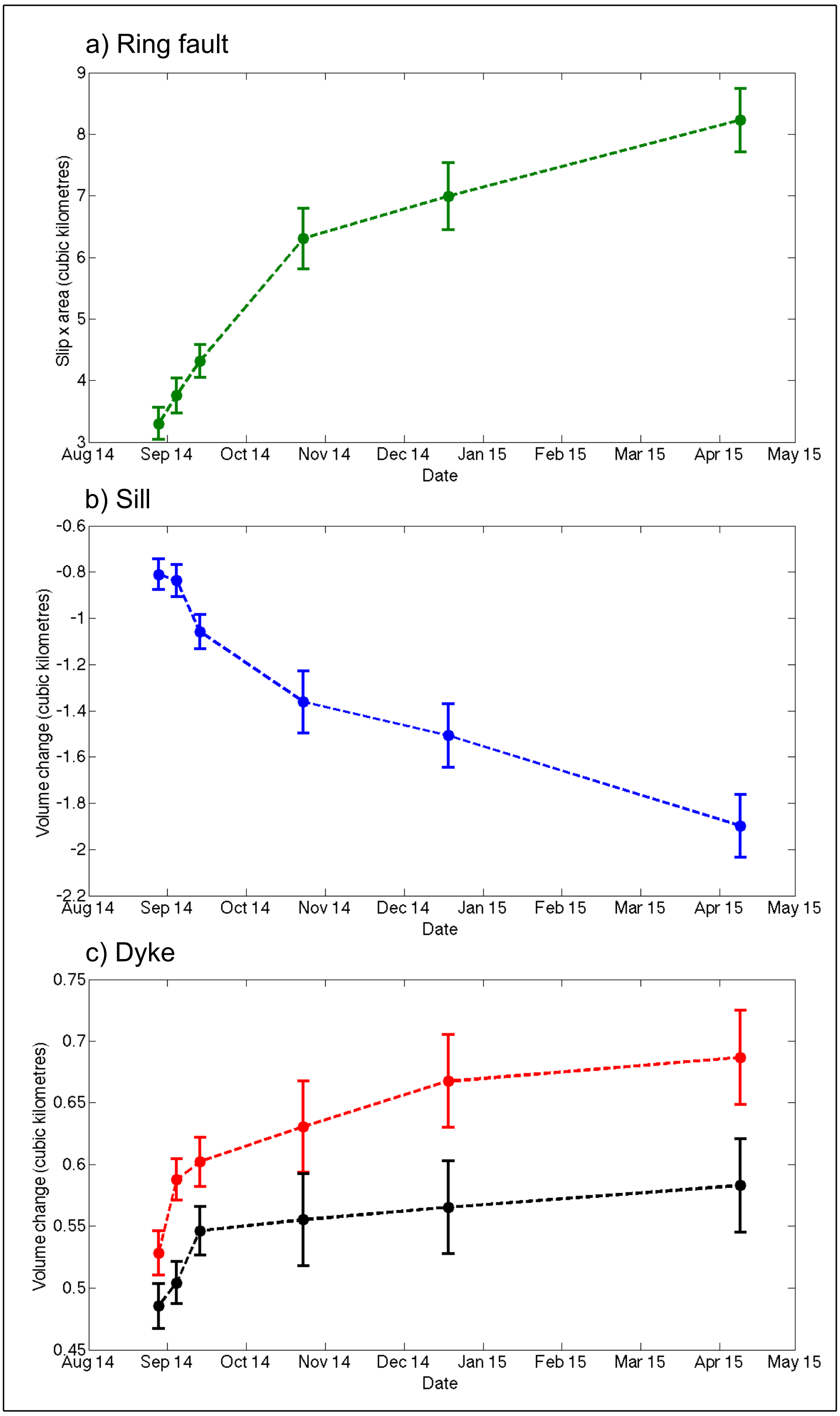

Figure 5. Time series of a) slip × area on the ring fault, b) closing × area of the sill and c) opening × area of the dyke. The red dashed line in c) represents the volume change computed from the optimal models. The blacked dashed line in c) represents the corrected volume change (see section 3 for details). The error bars represent the 95% confidence interval (± 2 standard deviations of the total volume change from 10,000 iterations).

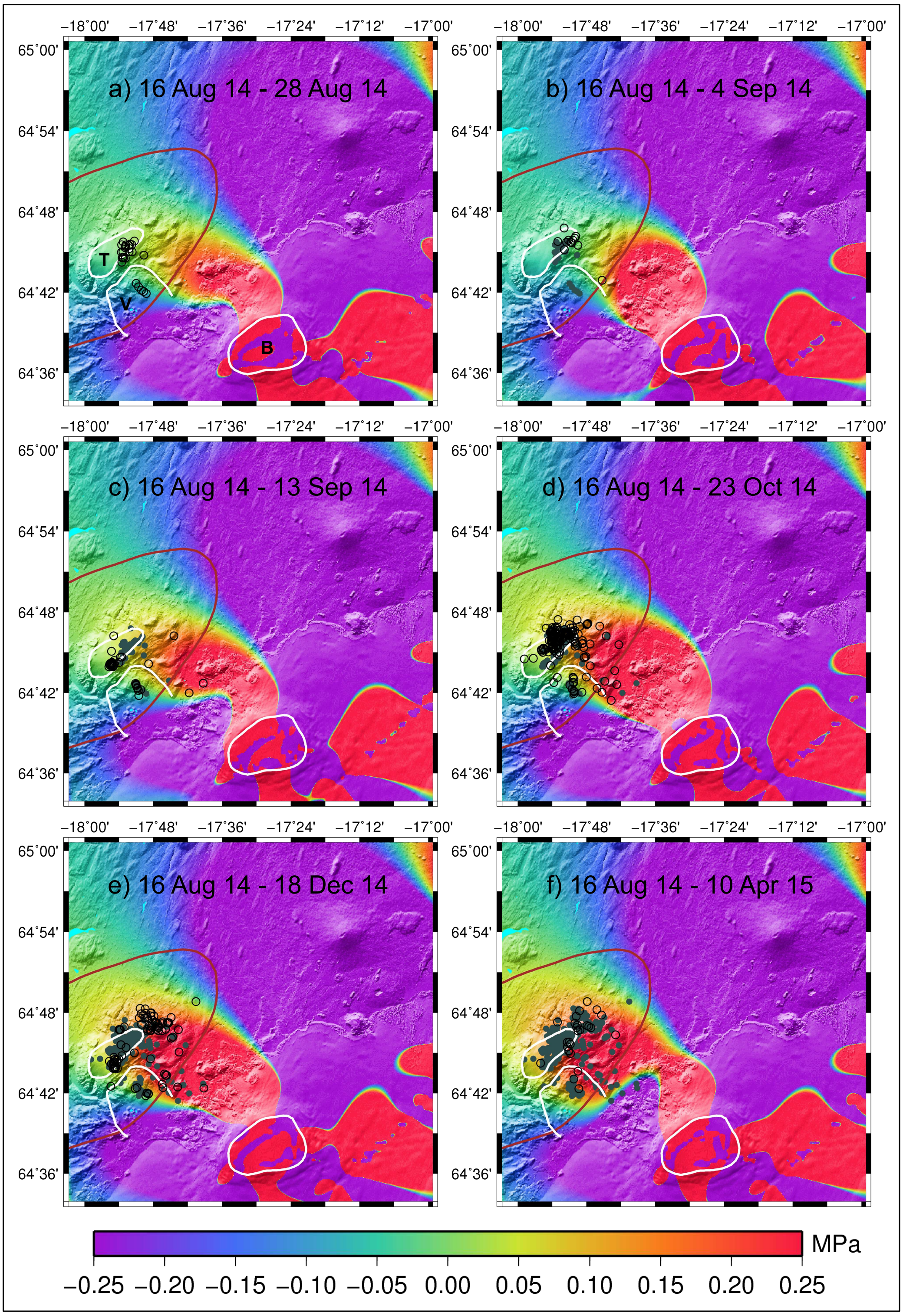

Figure 6. Cumulative Coulomb stress changes ($\Delta\sigma_c$) for depth interval 0-4 km. Red regions represent areas of increased $\Delta\sigma_{c,}$ assuming receiver faults that are normal faults with a strike of 220 degrees, dipping 55 degrees to the west. Underlying relief grid is the intermediate TanDEM-X DEM. Caldera outlines for Tungnafellsjökull (T), Vonarskard (V) and Bárdarbunga (B) are displayed in white. Outline of Tungnafellsjökull's fissure swarm is displayed in brown. New earthquakes (since end date in previous panel) are displayed as black open circles. Previous earthquakes (since the 16th August 2014) are displayed as filled grey circles.